Baseplate Temperature-Dependent Vertical Composition Gradient in Pseudo-Bilayer Films

for Printing Non-fullerene Organic Solar Cells

Yina Zheng[1†], Rui Sun[1†], Meng Zhang[2], Zhihao Chen[3], Zhengxing Peng[4*], Qiang Wu[1], Xinxin Yuan[1], Yue Yu[1], Tao Wang[1], Yao Wu[1], Xiaotao Hao[3], Guanghao Lu[2], Harald Ade[4*], Jie Min[1,5,6*]

[1]The Institute for Advanced Studies, Wuhan University, Wuhan 430072, China

E-mail: min.jie@whu.edu.cn

[2]Frontier Institute of Science and Technology, Xi'an Jiaotong University, Xi'an, 710054, China

[3]School of Physics, State Key Laboratory of Crystal Materials, Shandong University, Jinan, Shandong, 250100 P. R. China

[4]Department of Physics and Organic and Carbon Electronics Laboratories (ORaCEL) , North Carolina State University Raleigh, NC 27695, USA

E-mail: zpeng6@ncsu.edu; hwade@ncsu.edu

[5]Institute of Polymer Optoelectronic Materials and Devices, State Key Laboratory of Luminescent Materials and Devices, South China University of Technology, Guangzhou 510640, China

[6]Key Laboratory of Materials Processing and Mold, Ministry of Education, Zhengzhou University, Zhengzhou 450002, China

[†]These authors contributed equally

## Abstract

Numerous previous reports on sequential deposition (SD) technique have demonstrated that this approach can achieve a p-*i*-n active layer architecture with an ideal vertical composition gradient, which is one of the critical factors that can influence physical processes that determine the photovoltaic performance of organic solar cells. Herein, a commonly used photovoltaic system comprised of PM6 as a donor and Y6 as an acceptor is investigated with respect to sequential blade-processing deposition to comprehensively explore the morphology characteristics as a function of baseplate temperature. A systematic study of the temperature-dependent blend morphology elucidates the SD-processed configuration merits and device physics behind temperature-controlled degree of vertical composition gradient, and construct the temperature-microstructure-property relation to the corresponding photovoltaic parameters. The result shows, as the temperature increases, the morphology of the active layer has undergone a distinct evolution from pseudo-bulk heterojunction to pseudo-planar heterojunction and then to pseudo-planar bilayer, leading to a non-monotonic correlation between baseplate temperature and device performance. This investigation not only reveals the importance of precisely controlling baseplate temperature on gaining vertical morphology control, but also provides a path toward rational optimization of device performance in the lab-to-fab transition.

# 1. Introduction

Sequential deposition (SD) of the photoactive layers by solution processing for the first layer followed by the second layer (often the acceptor in an organic solar cell (OSC) device configuration, **Figure 1A**),[1-3] have gained considerable attention for its excellent compatibility with large-area blade-coating and the potential to realize scaled-up high-throughput manufacturing.[4] In comparison to the bulk heterojunction (BHJ) configuration formed by the deposition of donor: acceptor (D: A) mixtures with various blending weight ratios in solution state,[5-7] sequential deposition of the donor and acceptor independently as two separate processing steps offers a promising route towards commercial-scale fabrication of OSCs through numerous advantages.[8-11] Each material is deposited independently, allowing the control D-A compositional gradient and optimization of vertical and lateral phase distribution over discrete layers. Thus, compared to the common BHJ processing, this SD coating approach can facilitate more efficient formation of an optimized vertical phase separation,[12] greater control and optimization of D/A interfaces and more enhanced donor and acceptor aggregations at their respective electrodes in final morphology.[13-14] Of note is that small changes in BHJ processing conditions (such as solvent, additives, concentration, spin speed, drying time and so on),[8] operating ambient conditions (such as temperature, illumination and humidity)[15] or post-treatment steps

(including thermal annealing, solvent vapor annealing and two-step annealing, *etc*.)[16-17] can provoke a transition to another equilibrium state, inducing thermodynamically unfavourable blend morphology.[18-20] This indicates that vertical or lateral blend morphology that is formed during the film-formation BHJ might be a kinetics-limited state, and could be controlled by various external conditions and internal factors. In addition, often the thermodynamically favourable morphology does not yield preeminent device performance, requiring optimization of multiple experimental processing conditions to promote kinetic film formation.[21] Thus, the nature of D:A BHJ devices makes it challenging to predict and understand how changing one variable will influence the whole active layer morphology.[7, 21-22] In contrast, the SD processing is more robust,[9] with less dependence on the above-mentioned film-forming conditions.

Additionally, the pseudo-planar heterojunction (PPH) configuration, with an appropriate BHJ gradient in the middle of the active layer achieved by SD processing,[4, 9] generally exhibits a slightly red-shifted absorption spectra with a higher photo-absorption rate as compared to the BHJ blend.[10] It indicates that more number of photons in the SD-processed layer can be absorbed and converted into energy (extracted charges at electrodes).[9] Apart from the optical properties,[4, 9] the significant difference of BHJ and PPH morphologies influence the fundamental processes associated with the light-to-electrical energy conversion and charge collection. As compared with the corresponding BHJ blend, it was found that the PPH blend composed of polymer donor PM6[23-24] and non-fullerene acceptor (NFA) N3[24] possessed longer exciton diffusion length,[13, 25] and more efficient exciton diffusion, hole transfer channel and charge generation.[8-9] Further investigation found that the PPH blend shows the more efficient charge transport properties and less non-geminate recombination loss as compared to its BHJ counterpart.[9, 26-28] As a direct result, the obvious changes in the fundamental photo-physical processes between the complex BHJ and PPH active layer morphologies can effectively reflect the variations in the device performance trends.[9-10, 14] In

particular, many binary and ternary photovoltaic systems applied SD processing to controlling the vertical composition gradient and thus improving their photovoltaic performance with power conversion efficiencies (PCEs) of boosting to 17-18%.[11-13] More importantly, recent studies demonstrated that the SD process can effectively reduce the sensitivity of polymer batch,[29] suppress the scaling lag of OSC module efficiency,[30] and shows the diversity of solvent selection.[12, 31] In short, these advantages have resulted in significant interest in the SD technique and its potential to displace conventional BHJ as the dominant film-forming process for large-scale OSC manufacturing.[30, 32]

Although suitable vertical phase separation[11-13, 30] can be easily achieved by SD processing approach, the lack of control over vertical composition gradient and molecular crystallinity at the time of sequential blade-processing deposition probably remains a key limitation. Notably, unlike the development of a vertical composition gradient in a BHJ blend film during rapid solvent evaporation strongly and simultaneously affected by multiple key parameters, including the miscibility (or interaction parameter $\chi$) of the D/A components,[33] the molecular crystallinity,[4] free-surface or interfacial surface energy,[34-35]] and the abovementioned processing conditions,[15-16, 36] baseplate and solvent temperature, *etc*.,[7, 37-39] the major factor that affected the vertical phase separation in a PPH layer is the baseplate temperature during the printing technique progress.[8] In other words, the rate of solvent evaporation (or changes of film drying time) plays a vital role in influencing the vertical stratification in SD-processed films. However, the kinetics of morphology evolution especially in terms of the vertical phase separation processes during SD processing is not investigated in detail. Thus, understanding the temperature dynamic effects of SD processing on the morphology evolution especially in terms of the vertical and lateral morphology plays a vital role in developing high-performance material systems and facilitating the applications of SD technique in large-scale industrial OSC module manufacturing.[4]

In this work, we shed light on the correlation between photovoltaic performance and SD-processed morphology as a function of baseplate temperature *via* a doctor-blade coating process. The subject of this study is the commercially available PM6 (as a donor) and Y6[40] (as an acceptor, **Figure 1A**). The device performance of PM6/Y6 is extremely sensitive to the temperature of SD process using chloroform (CF) as solvent, and exhibits a nonmonotonic trend with the increase of baseplate temperature. The PPH blend fabricated at 45 °C exhibits optimal vertical composition gradient and thus yield the higher device performance than those of the SD-processed active layers prepared at lower or higher baseplate temperatures. To explain the nonmonotonic behavior of PCE with the increase of temperature which is implying that the composite undergoes a plurality of microstructure modifications, we further delineate the causative relations between active layer morphology and device performance of PM6/Y6 system. In particular, the detailed morphologies were categorized according to their electrooptical and electronic properties with the nonmonotonic behaviors.

## 2. Results and Discussion

A conventional device architecture, indium tin oxide (ITO)/poly (3,4-ethylene dioxythiophene):polystyrene sulfonate (PEDOT:PSS)/PM6/Y6/aliphatic amine-functionalized perylene-diimide (PDINN)[41]/Ag, was used to investigate the device performance as a function of baseplate temperature as depicted in **Figure 1A**. Different baseplate temperatures were employed to adjust the rate of solvent evaporation and the degree of acceptor deposition, and thus control the vertical composition gradients of active layers for optimizing the corresponding device performance. **Figure S1** exhibits the ultraviolet-visible (UV-*vis*) absorption spectra of PM6 and Y6 neat films, which present excellent optical complementarity. The absorption of the SD-processed active layers with various baseplate temperatures is presented in **Figure 1B**. As the baseplate temperature

increasing from 20 to 60 ℃, 18 nm redshift of Y6 characteristics peak was easily found in the inset image in **Figure 1B**, indicating the better-ordered stacking of Y6 molecules.[4]

The current density-voltage (*J-V*) curves of relevant solar cells recorded under simulated AM1.5G sun illumination (100 mW cm$^{-2}$) are provided in **Figure 1C**, with corresponding photovoltaic parameters and relevant film-thickness data summarized in **Table 1**. In addition, the information on series resistance ($R_s$) and shunt resistance ($R_{sh}$) extracted from the *J-V* curves is presented in **Table S1**. As shown in **Figure 1D**, baseplate temperature plays a key role in the resulting device efficiencies especially in terms of the short-circuit current density ($J_{sc}$) and fill factor (FF) values. With the baseplate temperature increasing from 20 to 45 ℃, the SD-processed device exhibits an improved PCE from 12.15% to 16.17% due to an increased $J_{sc}$ from 24.18 to 26.22 mA cm$^{-2}$ and a boosted FF from 59.50% to 73.52%. Further increasing in temperature from 45 to 60 ℃, the FF and $J_{sc}$ values as well as the PCEs decreased gradually. Of note is that the $J_{sc}$ values obtained from *J-V* curves are further verified by the external quantum efficiency (EQE) measurement (**Figure S2** and **Table 1**). In particular, unlike the EQE spectra of the SD-processed devices with low baseplate temperatures (20 and 30 ℃), the more obvious shoulder peaks resulting from the aggregations of Y6 molecules can be easily found in the EQE spectra of relevant devices with high processing temperatures (**Figure S2**). Additionally, the detailed photocurrent density ($J_{ph}$)-effective voltage ($V_{eff}$) curve measurements (**Figure S3**) were conducted to evaluate the charge dissociation probability ($P_{E,T}$, $P_{E,T} = J_{ph}/J_{sat}$, where $J_{sat}$ represent the saturated photocurrent).[19, 42] Compared with the SD-processed active layer fabricated at 20 ℃ ($P_{E,T}$ of 96.4%) and 60 ℃ ($P_{E,T}$ of 97.3%), the film fabricated at 45 ℃ exhibits a higher $P_{E,T}$ of 99.0%. This result indicates that the SD-processed active layer fabricated at 45 ℃ have more efficient charge dissociation and collection properties compared to those based on the other baseplate temperatures, which contributes to the higher $J_{sc}$ and FF values (**Table 1**).
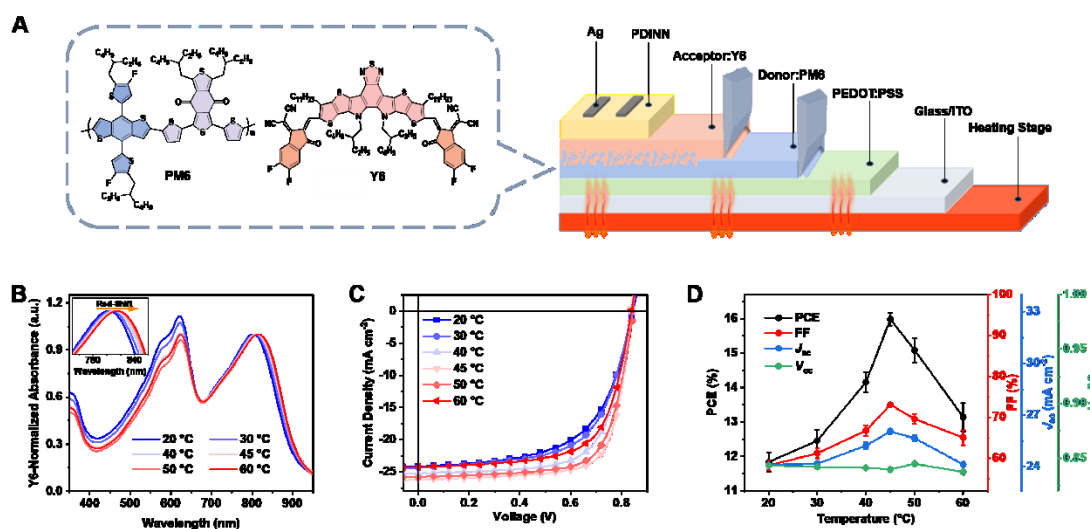
**Figure 1.** A) Chemical structures of PM6 and Y6, and schematic illustration of SD blade-coating approach as well as schematic device architecture of OSCs. B) Y6-Intensity-Normalized UV-*vis* absorption spectra of SD-processed PM6/Y6 bilayers fabricated at different baseplate temperatures. C) *J-V* curves of relevant SD-processed devices fabricated at different baseplate temperatures. D) Figures of merit of SD-processed solar cells as a function of substrate-temperature. Error bars represent plus or minus 1 standard deviation from the arithmetic mean value over eight devices.

**Table 1.** Detailed photovoltaic parameters of SD-processed PM6/Y6 devices fabricated at different temperatures under a 100 mW cm$^{-2}$ AM1.5G illumination and the corresponding film thicknesses of the neat and blend films.

| Baseplate Temperature [°C] | $V_{oc}$ [V] | $J_{sc}$ [mA cm$^{-2}$] | $J_{EQE}$[a] [mA cm$^{-2}$] | FF [%] | PCE$_{max}$ (PCE$_{ave}$[b]) [%] | Thickness[c] [nm] | Thickness[d] [nm] |
|---|---|---|---|---|---|---|---|
| 20 | 0.845 | 24.18 | 23.45 | 59.50 | 12.15 (11.84) | 54 | 103 |
| 30 | 0.841 | 24.31 | 24.01 | 62.52 | 12.78 (12.45) | 50 | 100 |
| 40 | 0.840 | 25.23 | 24.37 | 68.08 | 14.43 (14.15) | 45 | 98 |
| 45 | 0.839 | 26.22 | 25.01 | 73.52 | 16.17 (15.98) | 46 | 97 |
| 50 | 0.844 | 25.84 | 24.78 | 70.96 | 15.48 (15.08) | 51 | 101 |
| 60 | 0.838 | 24.23 | 23.83 | 66.94 | 13.59 (13.14) | 49 | 95 |

[a] The $J_{EQE}$ values obtained from the EQE spectra. [b] The average PCE obtained from eight devices. [c] The film thicknesses of neat PM6 layers fabricated at difference baseplate temperatures. [d] The film thicknesses of SD-processed PM6/Y6 bilayers fabricated at difference baseplate temperatures.

To directly reveal temperature-dependent microstructure evolution behind the film-forming process and understand the fundamentals of baseplate temperature-induced active layers, we conducted atomic force microscopy (AFM), film-depth-dependent light absorption spectroscopy (FLAS), time-of-flight secondary ion mass spectrometry (ToF-SIMS) measurements, resonant soft X-ray scattering (R-SoXS), and grazing incidence wide angle X-ray scattering (GIWAXS). AFM was firstly utilized to probe the surface morphology of the SD-processed PM6/Y6 films. **Figure S4** provides the corresponding AFM height sensor images. Notably, the AFM images of the various active layers as a function of baseplate temperature exhibited strong support and account for the optical absorption data (**Figure 1B**). Extending baseplate temperature from 20 to 60 °C leads to less rough films but significant phase separation and large domain size evaluated from the AFM images. It is because the solvent evaporation rate increases with the increase of baseplate temperature, which results in more Y6 molecules aggregate on the surface of the active layer without entering its bottom dramatically.

Before getting insight about the vertical morphology of the active layer, the information of D/A ratios for the entire bilayers were measured and provided in **Figure S5-S6** and **Table S2-S3**. The composition gradient of the corresponding sequentially deposited films was further analyzed *via* FLAS and ToF-SIMS techniques. First, FLAS technique was conducted for investigating the influence of temperature on vertical composition distribution and D/A mixed region comprehensively.[43] Here parameter $\beta$, which is calculated by the equation of $\beta = \sum_1^n |a - b_i|/n$ (where $n$ is the number of the sublayers), represents the homogeneity within active layer. Note that parameter $a$ and $b_i$, which can be derived from the film-depth light absorption profiles of the corresponding films (**Figure S7**), represent the ratio of the absorption peak of the Y6 and PM6 of the whole film and each sublayer, respectively ($a = Abs_{Y6}/Abs_{PM6}$; $b_i = Abs_{Y6}^i/Abs_{PM6}^i$, $i$ is the index of sublayer). When the baseplate temperature is approximately 20 °C, it can be seen that the evaporation of CF during film

formation is very slow. The difference in surface tension of PM6 (29.2 mN m$^{-1}$) and Y6 (30.6 mN m$^{-1}$) leads to the enrichment of Y6 near the bottom of active layer ($\beta$ = 0.133, see **Figure 2A** and **2B**).[44] Of note is that this vertical morphology is inferior for charge transport, which will be further analyzed below. In addition, increasing the baseplate temperature to 30 °C will accelerate the CF solvent evaporation process. Due to the balance between kinetics and thermodynamics of the film-forming process, donor and acceptor tend to distribute in the film homogeneously with $\beta$ decreasing to 0.119, which is close to the reference BHJ film ($\beta$ = 0.112, see **Figure 2A** and **2B**). This indicates that the SD-processed film fabricated at 30 °C tend to adopt a pseudo-BHJ architecture. However, we also note that the good performance of the BHJ film[4] is not directly evidenced by the comparable $\beta$ value of the pseudo-BHJ film fabricated by SD processing at 30 °C, which shows a PCE of 12.78%. This may be attributed to the different degree of phase separation and domain purity in these two types of active layers. Further extending the temperature from 30 to 45 °C, the SD-processed film exhibits a PPH architecture with different degrees of intermediate D:A blending phase, and the rising $\beta$ value illustrates the improved non-homogeneity. Notably, while the temperature reaches 50 °C (close to the boiling point of CF, 61.7 °C), the difference of $\beta$ between 50 °C (0.221) and 60 °C (0.222) is almost negligible, which imply the films tend to adopt relative pseudo-planar bilayer (PPB) architecture. This is due to the extremely short volatilization time of the CF solvent, which dramatically prevents Y6 molecules from being deposited into the PM6 phase domains.

The results from ToF-SIMS show good agreement with the evolution of film architecture indicated by FLAS technique. Here, ToF-SIMS is used to quantitatively monitor the vertical profiles of each component across the whole thickness of the corresponding SD-processed active layers. Notably, in PM6:Y6 system, CN$^-$ is a unique secondary ion belonging to Y6 and thus it can be used to track the distribution of Y6 throughout the films. As provided in **Figure 2C**, the SD-processed film fabricated at 30 °C shows a relatively uniform Y6 gradient

throughout the vertical active layer. Extending baseplate temperature from 30 to 45 °C and then to 60 °C results in more Y6 molecules to be deposited on the upper layer of the SD-processed active layers. Notably, temperature-dependent evolution of D/A vertical distribution depicted in the ToF-SIMS profiles further confirms the results of the optical absorption (**Figure 1B**), EQE spectra (**Figure S2**) and AFM images (**Figure S4**) as a function of varying baseplate temperatures. Although the vertical stratification of BHJ active layers during their film-formation process generally is a complex process resulting from the synergistic effects of many factors,[7, 9, 45-49] our results demonstrated that SD processing can more effectively control the vertical composition gradient of the active layer through baseplate temperature regulation because of the accelerated evaporation process of CF *via* the increase of the baseplate temperature.
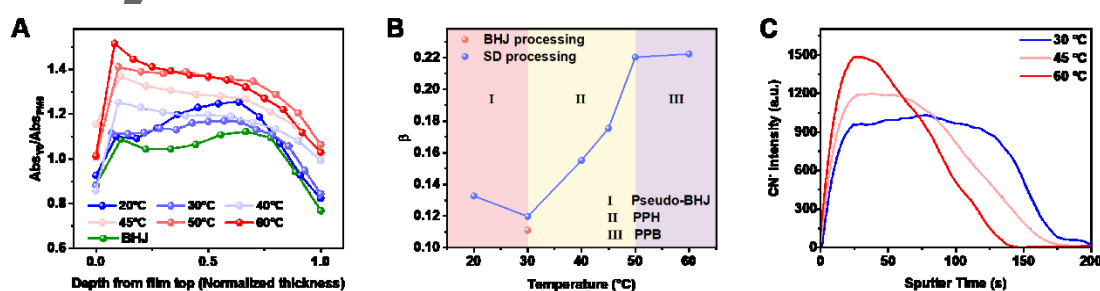


**Figure 2.** A) The ratio of absorption intensity between Y6 and PM6 as a function of the film depth. B) The $\beta$ value of the SD-processed films as a function of baseplate temperature and reference BHJ film. C) ToF-SIMS ion yield as a function of sputtering time (with a sputtering of 0.8 nm/s) for the SD-processed samples fabricated at different temperatures. The depth profile of Y6 by tracing CN⁻ is shown.

To investigate the film morphology at lateral scale, R-SoXS measurements were carried out to probe the scattering intensity and phase separation at multi-length scale.[50-52] A resonant energy of 288.8 eV was used to provide the material contrast between PM6 and Y6 and reduced fluorescence background. As shown in **Figure S8,** the R-SoXS profiles of films processed at temperatures lower than 45 °C show multi-length scale phase separation with two log-normal distributions located at a lower $q$ at ~0.05-0.1 nm$^{-1}$ and a higher $q$ at ~0.2-0.4

nm$^{-1}$, there is only a single low-$q$ peak for the device fabricated at 50-60 °C. The corresponding extracted parameters from the multi-peak fitting are shown in **Table 2** and **Figure 3**.[53-55] For the films processed at 30-45 °C (PPH architecture), the long period for both the larger domains (corresponding to the low-q peak) and the smaller domains (the high-q peak) increases as the baseplate temperature increases while the relative volume fraction of the larger domain and smaller domains remains almost unchanged (**Figure 3A** and **Figure 3B**). Moreover, due to the limitation of short exciton diffusion length (~20 nm), higher volume fraction of the smaller domain will facilitate exciton dissociation and enhance device performance.[3, 56] Compared with 20 °C (48% of the smaller domain), the device fabricated at 30-45 °C shows significant higher volume fraction of the smaller domain (70%-80%, **Figure 3B**) which is beneficial for charge generation. Further extending the temperature to 50-60 °C (PPB architecture) causes the vanishing of the high-$q$ peak and oversized domains (long period of 121.7 nm for 50 °C and 131.7 nm for 60 °C) would accelerate exciton recombination rate and lead to the poor photocurrent generation. Of note is that this result is also in agreement with the time-resolved transient photoluminescence (TRPL) and steady-state PL measurements, which will be discussed below. Compared with 50 °C, the device fabricated at 60 °C exhibits larger long period attributing to the reduced photovoltaic performance due to lacking of percolation pathways.[51] Since the R-SoXS scattering intensity of the corresponding lateral morphologies processed by high processing temperatures could not be probed, this hinders the evaluation of domain purity in relevant active layers processed by high temperatures (**Figure 3C**). In short, relative large domain size and high volume fraction of the high-$q$ peak as well as high domain purity all contribute to the optimal morphology of the PPH device fabricated at 45 °C, indicating the great potential of SD processing strategy of controlling the film morphology by baseplate temperature regulation.
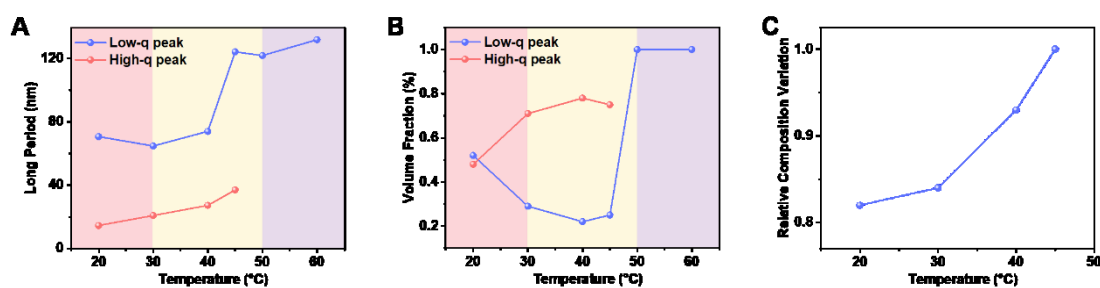
**Figure 3.** A) Long period of low-q peak and high-q peak as a function of baseplate temperatures. B) Relative volume fraction of low-q peak and high-q peak as a function of baseplate temperatures. C) Relative composition variation of lateral morphology as a function of baseplate temperatures.

**Table 2.** Correlative parameters of SD-processed devices fabricated at different temperatures

| Baseplate Temperature [°C] | Peak 1 (lower $q$) | | | Peak 2 (higher $q$) | | | Relative composition variation |
|---|---|---|---|---|---|---|---|
| | $q$ [nm$^{-1}$] | Long period [nm] | Relative volume fraction [%] | $q$ [nm$^{-1}$] | Long period [nm] | Relative volume fraction [%] | |
| 20 | 0.089 | 70.6 | 52 | 0.43 | 14.6 | 48 | 0.82 |
| 30 | 0.097 | 64.7 | 29 | 0.30 | 20.9 | 71 | 0.84 |
| 40 | 0.085 | 73.9 | 22 | 0.23 | 27.3 | 78 | 0.93 |
| 45 | 0.051 | 124.0 | 25 | 0.17 | 37.0 | 75 | 1 |
| 50 | 0.052 | 121.7 | 100 | | | | |
| 60 | 0.048 | 131.7 | 100 | | | | |

obtained from multipeak fitting of R-SoXS profiles.

We further conducted GIWAXS measurements to probe molecular ordering within the active layer (**Figure 4A**).[57-58] The 1D scattering profiles in **Figure 4B** show that all the lamellar stacking peaks of both PM6 and Y6 can be accordingly observed, suggesting that PM6 and Y6 can maintain their independent molecular packing, and the intensity of Y6 (010) peak dominates the π-π stacking. The extracted parameters (e.g., the stacking distance and coherence length) of π-π stacking are summarized in **Table S4**, and there is no distinct difference between various processing temperatures. Importantly, the molecular orientation distribution has notable impacts on the D/A orbital coupling strength, and therefore affect the device performance.[59] The Ewald sphere corrected pole figures for lamellar (100) peak are

shown in **Figure 4C** and the relative detailed description are shown in the **Table S5**[24, 60-61]. The face-on to edge-on ratios of the PPH films increase from 30 ℃ to 45 ℃ and then decrease at 50 ℃ (**Table S5**) with the maximum of 8.85 at 45 ℃. It is worth noting that improved potion of face-on with respect to the substrate at 45 ℃ will lead to the more favorable morphology with higher exciton dissociation efficiency and less recombination losses as compared to the other blend morphologies.[34, 62]
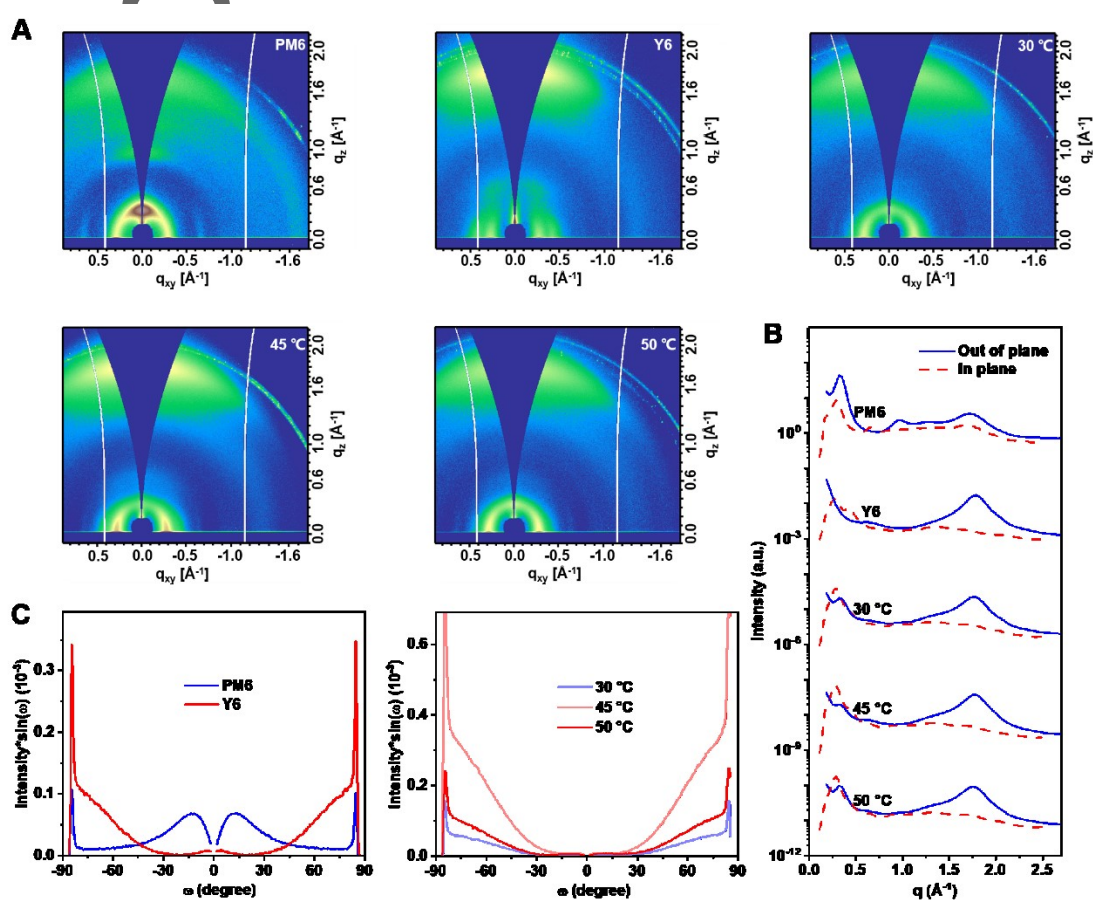


**Figure 4.** A) 2D-GIWAXS patterns of PM6, Y6 and SD-processed PM6/Y6 films fabricated at different temperatures. B) Corresponding 1D scattering profiles with respect to in-plane (IP) and out-of-plane (OOP) directions, acquired at the critical incident angle of 0.14°. C) Corresponding pole figures extracted from (100) scattering peaks, where ω is azimuthal angle between the crystallite orientation and the substrate normal with respect to the $q_z$ axis.

To further evaluate and discuss the relationships between blend morphology, photovoltaic parameters and physical dynamics, we investigated the photo-excited states and charge

carrier dynamics in these SD-processed blends by TRPL, steady-state PL, space charge limited current (SCLC), light intensity dependence of *J-V* characteristics, transient photovoltage (TPV), transient photocurrent (TPC) and photo-induced charge carrier extraction by linearly increasing voltage (photo-CELIV) measurements, and probably give a real inspiration of precisely controlling the optimal active layer morphology. In particular, our morphological measurements make clear the temperature-dependent evolution of lateral morphology and vertical phase separation as well as the D/A mixed region in SD-processed active layers, which is a critical parameter for exciton diffusion and dissociation. As shown in **Figure 5A**, as the baseplate temperature increases from 30 to 60 ℃, the PL intensity in the SD-processed films undergo a monotonic improvement. A strong quenching of the PL intensity is observed in the film fabricated at 30 ℃ when compared with films of pristine Y6, resulting from the dominantly amorphous intermixing BHJ. Upon increasing of baseplate temperatures, the PL intensity is partially recovered proportionally to the increase in vertical phase separation. As compared to the PPH film fabricated at 45 ℃, the recovery of PL intensity is stronger for the SD-processed film fabricated at 60 ℃ indicating its less efficient exciton dissociation due to the inferior D/A interfacial area hold by the PPB architecture. Note that the TRPL studies, as shown in **Figure 5B** along with the detailed description in the **Table S6**, also confirmed the temperature-dependent evolution of exciton dissociation in SD-processed active layers. The TRPL signal in the film fabricated at 30 ℃ decay fast with $\tau$ of 45 ps, which is much faster than those of the high-temperature processed PM6/Y6 films ($\tau$ = 58 ps for the film fabricated at 45 ℃ and $\tau$ = 68 ps for the film fabricated at 60 ℃) and the pristine film Y6 ($\tau$ = 545 ps). Therefore, these PL results are in excellent agreement with the abovementioned morphological characteristics.

Of particular note is that, as compared to the PPH film fabricated at 45 ℃, the pseudo-BHJ film fabricated at 30 ℃ possesses the better exciton dissociation, but its device exhibits the lower $J_{sc}$ and FF values. This result may be mainly contributed to its poor charge transport

and extraction properties as well as non-geminate recombination losses in devices.[55] To demonstrate this hypothesis, we further carried out the SCLC measurements[5, 55] to determine the hole and electron mobility (**Figure S9** and **Figure S10**) and their corresponding results are provided in **Figure 5C** and **Table 3**, respectively. The hole and electron mobilities of the pseudo-BHJ film were $1.79 \times 10^{-4}$ and $1.54 \times 10^{-4}$ cm$^2$V$^{-1}$s$^{-1}$, respectively. Both hole and electron mobilities can be improved significantly with the increase of the baseplate temperature from 30 to 45 °C. The corresponding SCLC devices fabricated at 45 °C show a hole-only mobility of $3.91 \times 10^{-4}$ cm$^2$V$^{-1}$s$^{-1}$ and an electron-only mobility of $3.79 \times 10^{-4}$ cm$^2$V$^{-1}$s$^{-1}$, respectively. Note that the PPB film fabricated at 60 °C shows lower hole and electron mobilities (a $\mu_h$ of $1.07 \times 10^{-4}$ cm$^2$V$^{-1}$s$^{-1}$ and a $\mu_e$ of $1.76 \times 10^{-4}$ cm$^2$V$^{-1}$s$^{-1}$, see **Table 3**) as compared to the other two SD-processed films. This only can be explained by a well ordered two phase microstructure with little relevance of the amorphous D:A mixed regimes. More acceptor materials were enriched on the top of the PPB film, which lead to the lacking of percolation pathways and therefore, and can inevitably suppress the delivery of carriers.[9] Additionally, the photo-CELIV technique was employed to investigate the carrier mobility in relevant devices (**Figure 5D**). As compared to the devices fabricated at 30 and 60 °C, the device fabricated at 45 °C exhibits a higher photo-generated carrier density of $6.05 \times 10^{13}$ cm$^{-3}$ while maintaining a higher device mobility of $1.56 \times 10^{-4}$ cm$^2$V$^{-1}$s$^{-1}$ calculated from the **Figure S11**. Notably, the device fabricated at 60 °C shows lower carrier density ($5.22 \times 10^{13}$ cm$^{-3}$), mainly resulting from the large domain size and limited D/A interface.[63] Photo-CELIV measurements strongly underpin the findings from PL and SCLC studies and, highlights the fact that the PPH film fabricated at 45 °C exhibits the better device performance as compared to the other SD-processed films.

**Figure S12** shows the TPV signal of the corresponding SD-processed devices at different light intensity (from 0.1 to 2.1 suns), which reveals the decay rate of photo-generated charge density in microsecond scale measured at approximately open circuit. And the charge carrier

lifetime of OSCs can be calculated from TPV for evaluating the recombination loss.[64] As the corresponding parameters shown in **Figure 5E** and **Table 3**, the carrier lifetime shows a non-monotonic trend with temperature. As the temperature increases from 30 to 45 °C, the carrier lifetime of PPH-based device increased from 4.0 to 10.9 μs. Note that this result confirms a significantly slower non-geminate recombination in the PPH device fabricated at 45 °C, which is probably related to the increased vertical phase separation and improved molecular ordering. Further extending the baseplate temperature to 60 °C will suppress the device performance with shorter carrier lifetime because of the larger domain sizes but inferior carrier transport pathway.[55] Additionally, we analyzed the charge extraction properties of relevant devices at $J_{sc}$ condition (**Figure S13**). The SD-processed device fabricated at 45 °C exhibits the shortest charge extraction time calculated from the TPC measurements among these three types of devices (**Figure 5E** and **Table 3**). This result further demonstrates its highly-efficient carrier transport pathway and suppressed non-geminate recombination loss, which agrees with the better photovoltaic performance of the devices fabricated at 45 °C. Besides, the investigation of the $V_{oc}$ versus light intensity curves of the corresponding devices fabricated at different baseplate temperatures also demonstrates the abovementioned physical results. As shown in **Figure 5F**, the device fabricated at 45 °C shows the smallest slope of 1.30 $k_B T/q$ among these three types of devices, which implies less trap-assisted recombination loss and better percolation pathways in the PPH active layer as compared with the pseudo-BHJ and PPB blends.
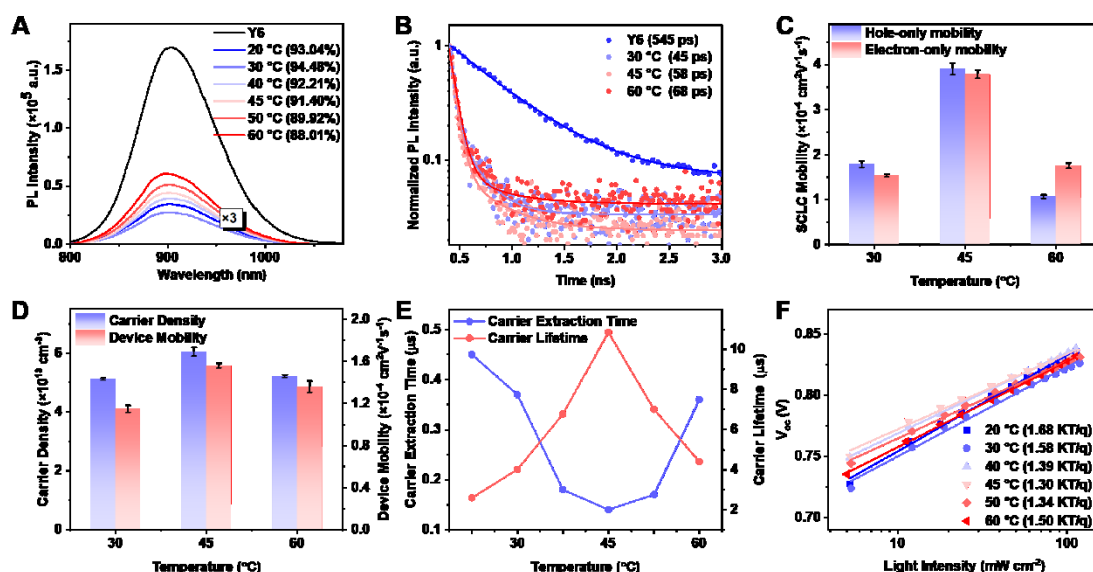
**Figure 5.** A) PL spectra of Y6 and SD-processed PM6/Y6 films fabricated at different temperatures under 639 nm photo-excitation. Note: PL data of SD-processed films were multiplied by 3 to display on the absolute intensity scale. B) Normalized decays of the PL intensity of Y6 film and corresponding SD-processed films fabricated at different temperatures taken at maximum emission. All films were excited at 400 nm. C) Averaged hole-only mobility and electron-only mobility measured in single-carrier diodes obtained from PM6/Y6 blends fabricated at different temperatures. For the SCLC measurements, the values were obtained based on eight devices of each type. D) Carrier density and device mobility and E) carrier extraction time and carrier lifetime of the relevant devices versus baseplate temperature. F) $V_{oc}$ of devices fabricated at different temperatures plotted against light intensity on a logarithmic scale, together with linear fits to the data (solid lines). The fitting formula used here can be described as: $V_{oc} = \frac{nk_BT}{q}lnP_{in}$, where $k_B$ is Boltzmann constant, $T$ is absolute temperature, $q$ is elementary charge.[8, 65]

**Table 3.** Corresponding parameters of the SD-processed PM6/Y6 devices fabricated at various temperatures obtained from different measurements.

| Temperature [°C] | $\Phi_q$ [a)] [%] | $\tau$ [b)] [ps] | $\mu_h$ [c)] [cm$^2$V$^{-1}$s$^{-1}$] | $\mu_e$ [d)] [cm$^2$V$^{-1}$s$^{-1}$] | $\mu_h/\mu_e$ | $\mu$ [e)] [cm$^2$V$^{-1}$s$^{-1}$] | $n$ [f)] [cm$^{-3}$] | $\tau$ [g)] [μs] | $\tau$ [h)] [μs] |
|---|---|---|---|---|---|---|---|---|---|
| 30 | 94.48 | 45 | 1.79×10$^{-4}$ | 1.54×10$^{-4}$ | 1.16 | 1.15×10$^{-4}$ | 5.12×10$^{13}$ | 0.37 | 4.0 |
| 45 | 91.40 | 58 | 3.91×10$^{-4}$ | 3.79×10$^{-4}$ | 1.03 | 1.56×10$^{-4}$ | 6.05×10$^{13}$ | 0.14 | 10.9 |

| 60 | 88.01 | 68 | $1.07\times10^{-4}$ | $1.76\times10^{-4}$ | 0.61 | $1.36\times10^{-4}$ | $5.22\times10^{13}$ | 0.36 | 4.4 |

a)The quenching efficiency calculated from the steady-state PL measurements. b)The PL quenching lifetimes calculated from the time-resolved transient PL measurements. c)The average hole mobility calculated from the SCLC measurements. d)The average electron mobility calculated from the SCLC measurements. e)The device mobility calculated by photo-CELIV measurements. f)The photo-generated carrier density calculated by photo-CELIV measurements. g)The carrier extraction time calculated from the TPC measurements. h)The carrier lifetime calculated from the TPV measurements under one sun illumination.

Based on all these investigations we derive a simplified picture for the morphology evolution as a function of baseplate temperature. As depicted in **Figure 6**, different baseplate temperature conditions evoke various degrees of vertical composition gradient in the SD-processed films, and thus resulting in three types of film architectures, including pseudo-BHJ, PPH and PPB. In details, processing at the low temperatures (below 30 °C), solvent volatilization has been prolonged and more PM6 molecules are swollen in the Y6 solution, and strong D/A intermixed photoactive layer tend to adopt pseudo-BHJ architecture, with a small domain size as consequence. This leads to a high exciton dissociation efficiency, but at the costs of considerable geminate and nongeminate recombination losses as well as inferior charge transport and extraction properties. As a direct result, $J_{sc}$ and FF values in relevant devices are dramatically impacted by such an intermixed microstructure, leading to the poor photovoltaic performance (**Table 1**). While increasing the processing temperature from 30 to 45 °C will certainly accelerate the film forming process. In particular, the film fabricated at 45 °C exhibited an optimal PPH architecture with increasing phase separation and domain purity which is favorable for the charge transport and carrier extraction properties, resulting in higher $J_{sc}$ and FF values in these devices. Apart from these merits, the PPH-based devices also possessed longer carrier lifetime and the shorter charge extraction time as compared to the pseudo-BHJ- and PPB-based devices, thus leading to the optimal photovoltaic performance. The film tends to form PPB architecture as further extending the temperature to 50-60 °C (**Figure 6**). As mentioned above, although the PPB architecture

exhibits the better exciton diffusion length, the investigated recovery of PL intensity indicates that the PPB film possesses less efficient dissociation due to the inferior D/A interfacial area, supported by the abovementioned morphology characterizations. Since the lacking of percolation pathways can inevitably suppress the carrier transportation, the PPB-based devices fabricated at 50-60 °C generally showed the inferior charge transport, less carrier density, higher non-geminate recombination loss, and shorter carrier lifetime as compared to the PPH-based devices, which agrees with the worse $J_{sc}$ and FF values of the SD-processed devices fabricated at relative high temperatures (**Table 1**).

In short, this model for the morphology evolution as a function of baseplate temperature is consistent to all our morphological characterizations. In particular, the results of the carrier dynamic analysis coupled with the exciton dissociation analysis finally complement the abovementioned investigations of the morphology characterizations and give detailed insight into subtle mechanisms being responsible for the observed performance trends as a function of baseplate temperatures. Impressively, the choice of baseplate temperatures based on SD-processed technique enables effectively fine-tuning the vertical phase separation, D/A interfacial area, molecular ordering and domain purity, and thus changing the fundamental photo-physical processes of SD-processed blends as well as their device performance. Thus, unlike the deposition technique of the D:A mixture (the BHJ blend formed by this processing approach is affected by multiple factors as mentioned above), in the SD technique, it can be seen that the baseplate temperature during the printing technique progress is a key factor in the formation of an optimal PPH architecture. Consequently, the SD-processed device fabricated at 45 °C can obtain the optimal vertical and lateral morphology which alleviate the trade-off of fundamental processes in the PPH blend compared with the active layers fabricated at other processing temperatures. From the abovementioned investigations, we provide a schematic summary (**Figure 6**) insight into the temperature-dependent morphological characteristics and its relation to the observed trade-offs in fundamental

mechanisms and device performance. While we can conclude that SD processing approach primarily acts as a plasticizer to enable ripening of the vertical phase separation with an optimal p-*i*-n like structure.
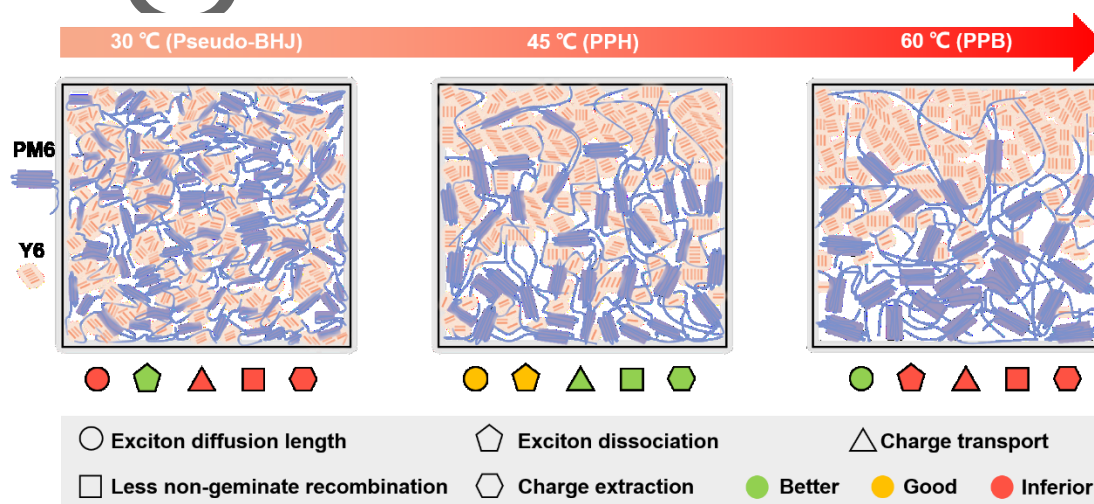


**Figure 6.** The evolution of morphological characteristics and fundamental processes as a function of baseplate temperature.

## 3. Conclusion

In summary, we employ sequential blade-coating deposition to systematically study the impact of baseplate temperature on the photovoltaic performance of PM6/Y6 devices. Films fabricated at 45 °C showed maximum performance, which is much higher than those of the SD-fabricated at higher or lower baseplate temperatures. In-depth study of microstructure variations under various baseplate temperatures were conducted by multi-scale morphological characterization techniques to investigate differences in device performance with respective to fundamental photo-physical processes in parallel. We claimed that three SD-processed active layer architectures with distinct microstructure characteristics, including pseudo-BHJ, PPH and PPB, were identified for PM6/Y6 as a function of baseplate temperature. In addition, electro-optical and electronic characterizations were performed to

shed light on the exciton dissociation and carrier dynamics, which finally could explain the observed performance trends due to the morphological variations of the corresponding active layers processed with different temperatures. All these results illustrate that optimizing SD-processed device performance *via* tuning baseplate temperature is a simple and feasible method. More detailed insight into baseplate temperature factor may lead to improved material and device specifications for the corresponding processing solvents, additives, solution concentrations, shearing speed, drying time, ambient conditions, *etc*., and to better processing control for organic solar cells and other organic electronic devices (e.g., organic photodetector[66]).

**Supporting Information**

Supporting Information is available from… or from the author.

**Conflict of Interest**

The authors declare no conflict of interest.

**Keywords**

organic solar cells, sequential deposition technology, processing temperature, D/A mixed region, morphology evolution

**References**

[1]     A. L. Ayzner, C. J. Tassone, S. H. Tolbert, B. J. Schwartz, *J. Phys. Chem. C* **2009**, 113, 20050.

[2]     Y. Lin, L. Ma, Y. Li, Y. Liu, D. Zhu, X. Zhan, *Adv. Energy Mater.* **2014**, 4, 1300626.

[3]     Y. Wang, X. Zhan, *Adv. Energy Mater.* **2016**, 6, 1600414.

[4]     R. Sun, Q. Wu, J. Guo, T. Wang, Y. Wu, B. Qiu, Z. Luo, W. Yang, Z. Hu, J. Guo, M. Shi, C. Yang, F. Huang, Y. Li, J. Min, *Joule* **2020**, 4, 407.

[5]     R. Sun, W. Wang, H. Yu, Z. Chen, X. Xia, H. Shen, J. Guo, M. Shi, Y. Zheng, Y. Wu, W. Yang, T. Wang, Q. Wu, Y. Yang, X. Lu, J. Xia, C. J. Brabec, H. Yan, Y. Li, J. Min, *Joule* **2021**, 5, 1548.

[6]     Q. Li, L.-M. Wang, S. Liu, L. Guo, S. Dong, G. Ma, Z. Cao, X. Zhan, X. Gu, T. Zhu, Y.-P. Cai, F. Huang, *ACS Energy Lett.* **2020**, 5, 3637.

[7]     Q. Wang, Y. Qin, M. Li, L. Ye, Y. Geng, *Adv. Energy Mater.* **2020**, 10, 2002572.

[8]     R. Sun, J. Guo, C. Sun, T. Wang, Z. Luo, Z. Zhang, X. Jiao, W. Tang, C. Yang, Y. Li, J. Min, *Energy Environ. Sci.* **2019**, 12, 384.

[9]     R. Sun, J. Guo, Q. Wu, Z. Zhang, W. Yang, J. Guo, M. Shi, Y. Zhang, S. Kahmann, L. Ye, X. Jiao, M. A. Loi, Q. Shen, H. Ade, W. Tang, C. J. Brabec, J. Min, *Energy Environ. Sci.* **2019**, 12, 3118.

[10]    Q. Wu, W. Wang, Y. Wu, Z. Chen, J. Guo, R. Sun, J. Guo, Y. Yang, J. Min, *Adv. Funct. Mater.* **2021**, 31, 2010411.

[11]    L. Zhan, S. Li, X. Xia, Y. Li, X. Lu, L. Zuo, M. Shi, H. Chen, *Adv. Mater.* **2021**, 33, 2007231.

[12]   Y. Wei, J. Yu, L. Qin, H. Chen, X. Wu, Z. Wei, X. Zhang, Z. Xiao, L. Ding, F. Gao, H. Huang, *Energy Environ. Sci.* **2021**, 14, 2314.

[13]   K. Jiang, J. Zhang, Z. Peng, F. Lin, S. Wu, Z. Li, Y. Chen, H. Yan, H. Ade, Z. Zhu, A. K. Jen, *Nat. Commun.* **2021**, 12, 468.

[14]   H. C. Wang, P. Cheng, S. Tan, C. H. Chen, B. Chang, C. S. Tsao, L. Y. Chen, C. A. Hsieh, Y. C. Lin, H. W. Cheng, Y. Yang, K. H. Wei, *Adv. Energy Mater.* **2021**, 11, 2003576.

[15]   F. Zhao, H. Zhang, R. Zhang, J. Yuan, D. He, Y. Zou, F. Gao, *Adv. Energy Mater.* **2020**, 10, 2002746.

[16]   J. Min, X. Jiao, V. Sgobba, B. Kan, T. Heumüller, S. Rechberger, E. Spiecker, D. M. Guldi, X. Wan, Y. Chen, H. Ade, C. J. Brabec, *Nano Energy* **2016**, 28, 241.

[17]   Y. Qin, Y. Xu, Z. Peng, J. Hou, H. Ade, *Adv. Funct. Mater.* **2020**, 30, 2005011.

[18]   M. Ghasemi, N. Balar, Z. Peng, H. Hu, Y. Qin, T. Kim, J. J. Rech, M. Bidwell, W. Mask, I. McCulloch, W. You, A. Amassian, C. Risko, B. T. O'Connor, H. Ade, *Nat. Mater.* **2021**, 20, 525.

[19]   W. Yang, W. Wang, Y. Wang, R. Sun, J. Guo, H. Li, M. Shi, J. Guo, Y. Wu, T. Wang, G. Lu, C. J. Brabec, Y. Li, J. Min, *Joule* **2021**, 5, 1209.

[20]   M. Ghasemi, H. Hu, Z. Peng, J. J. Rech, I. Angunawela, J. H. Carpenter, S. J. Stuard, A. Wadsworth, I. McCulloch, W. You, H. Ade, *Joule* **2019**, 3, 1328.

[21]   F. Zhao, C. Wang, X. Zhan, *Adv. Energy Mater.* **2018**, 8, 1703147.

[22]   A. Karki, A. J. Gillett, R. H. Friend, T. Q. Nguyen, *Adv. Energy Mater.* **2020**, 11, 2003441.

[23]   M. Zhang, X. Guo, W. Ma, H. Ade, J. Hou, *Adv. Mater.* **2015**, 27, 4655.

[24]   K. Jiang, Q. Wei, J. Y. L. Lai, Z. Peng, H. K. Kim, J. Yuan, L. Ye, H. Ade, Y. Zou, H. Yan, *Joule* **2019**, 3, 3020.

[25]   T. H. Lee, S. Y. Park, W.-W. Park, X. Du, J. H. Son, N. Li, O.-H. Kwon, H. Y. Woo, C. J. Brabec, J. Y. Kim, *ACS Energy Lett.* **2020**, 5, 1628.

[26]   Q. He, W. Sheng, M. Zhang, G. Xu, P. Zhu, H. Zhang, Z. Yao, F. Gao, F. Liu, X. Liao, Y. Chen, *Adv. Energy Mater.* **2021**, 11, 2003390.

[27]    J. Zhang, M. H. Futscher, V. Lami, F. U. Kosasih, C. Cho, Q. Gu, A. Sadhanala, A. J. Pearson, B. Kan, G. Divitini, X. Wan, D. Credgington, N. C. Greenham, Y. Chen, C. Ducati, B. Ehrler, Y. Vaynzof, R. H. Friend, A. A. Bakulin, *Adv. Energy Mater.* **2019**, 9, 1902145.

[28]    Y. Li, Y. Lin, *J. Mater. Chem. C* **2021**, DOI: 10.1039/d1tc01536b.

[29]    K. Weng, L. Ye, L. Zhu, J. Xu, J. Zhou, X. Feng, G. Lu, S. Tan, F. Liu, Y. Sun, *Nat. Commun.* **2020**, 11, 2855.

[30]    S. Liu, D. Chen, X. Hu, Z. Xing, J. Wan, L. Zhang, L. Tan, W. Zhou, Y. Chen, *Adv. Funct. Mater.* **2020**, 30, 2003223.

[31]    L. Ye, Y. Xiong, Z. Chen, Q. Zhang, Z. Fei, R. Henry, M. Heeney, B. T. O'Connor, W. You, H. Ade, *Adv. Mater.* **2019**, 31, 1808153.

[32]    M. D. M. Faure, B. H. Lessard, *J. Mater. Chem. C* **2021**, 9, 14.

[33]    L. Ye, S. Li, X. Liu, S. Zhang, M. Ghasemi, Y. Xiong, J. Hou, H. Ade, *Joule* **2019**, 3, 443.

[34]    J. Wang, Z. Zheng, D. Zhang, J. Zhang, J. Zhou, J. Liu, S. Xie, Y. Zhao, Y. Zhang, Z. Wei, J. Hou, Z. Tang, H. Zhou, *Adv. Mater.* **2019**, 31, 1806921.

[35]    R. Sun, D. Deng, J. Guo, Q. Wu, J. Guo, M. Shi, K. Shi, T. Wang, L. Xue, Z. Wei, J. Min, *Energy Environ. Sci.* **2019**, 12, 2518.

[36]    L. J. Richter, D. M. DeLongchamp, A. Amassian, *Chem. Rev.* **2017**, 117, 6332.

[37]    W. Yang, J. Guo, R. Sun, J. Yang, M. Shi, Q. Bao, J. Min, *Sol. RRL* **2019**, 3, 1900166.

[38]    N. Wang, Y. Yu, R. Zhao, Z. Ding, J. Liu, L. Wang, *Macromolecules* **2020**, 53, 3325.

[39]    E. F. Manley, J. Strzalka, T. J. Fauvell, N. E. Jackson, M. J. Leonardi, N. D. Eastham, T. J. Marks, L. X. Chen, *Adv. Mater.* **2017**, 29, 1703933.

[40]    J. Yuan, Y. Zhang, L. Zhou, G. Zhang, H.-L. Yip, T.-K. Lau, X. Lu, C. Zhu, H. Peng, P. A. Johnson, M. Leclerc, Y. Cao, J. Ulanski, Y. Li, Y. Zou, *Joule* **2019**, 3, 1140.

[41]    J. Yao, B. Qiu, Z. G. Zhang, L. Xue, R. Wang, C. Zhang, S. Chen, Q. Zhou, C. Sun, C. Yang, M. Xiao, L. Meng, Y. Li, *Nat. Commun.* **2020**, 11, 2726.

[42]    Y. Chen, R. Ma, T. Liu, Y. Xiao, H. K. Kim, J. Zhang, C. Ma, H. Sun, F. Bai, X. Guo, K. S. Wong, X. Lu, H. Yan, *Adv. Energy Mater.* **2021**, 11, 2003777.

[43]    X. Feng, Y. Wang, T. Xiao, Z. Shen, Y. Ren, G. Lu, L. Bu, *Front. Chem.* **2020**, 8, 211.

[44]    Q. An, J. Wang, X. Ma, J. Gao, Z. Hu, B. Liu, H. Sun, X. Guo, X. Zhang, F. Zhang, *Energy Environ. Sci.* **2020**, 13, 5039.

[45]    D. Yang, F. C. Löhrer, V. Körstgens, A. Schreiber, B. Cao, S. Bernstorff, P. Müller-Buschbaum, *Adv. Sci.* **2020**, 7, 2001117.

[46]    H. Yan, Y. Tang, X. Sui, Y. Liu, B. Gao, X. Liu, S. F. Liu, J. Hou, W. Ma, *ACS Energy Lett.* **2019**, 4, 1356.

[47]    H. Lee, C. Park, D. H. Sin, J. H. Park, K. Cho, *Adv. Mater.* **2018**, 30, e1800453.

[48]    E. F. Manley, J. Strzalka, T. J. Fauvell, T. J. Marks, L. X. Chen, *Adv. Energy Mater.* **2018**, 8, 1800611.

[49]    A. A. Mannanov, V. V. Bruevich, E. V. Feldman, V. A. Trukhanov, M. S. Pshenichnikov, D. Y. Paraschuk, *J. Phys. Chem. C* **2018**, 122, 19289.

[50]    L. Ye, B. A. Collins, X. Jiao, J. Zhao, H. Yan, H. Ade, *Adv. Energy Mater.* **2018**, 8, 1703058.

[51]    E. Gann, A. T. Young, B. A. Collins, H. Yan, J. Nasiatka, H. A. Padmore, H. Ade, A. Hexemer, C. Wang, *Rev Sci Instrum* **2012**, 83, 045110.

[52]    B. A. Collins, Z. Li, J. R. Tumbleston, E. Gann, C. R. McNeill, H. Ade, *Adv. Energy Mater.* **2013**, 3, 65.

[53]    S. Mukherjee, C. M. Proctor, G. C. Bazan, T.-Q. Nguyen, H. Ade, *Adv. Energy Mater.* **2015**, 5, 1500877.

[54]    S. Mukherjee, C. M. Proctor, J. R. Tumbleston, G. C. Bazan, T. Q. Nguyen, H. Ade, *Adv. Mater.* **2015**, 27, 1105.

[55]    J. Min, X. Jiao, I. Ata, A. Osvet, T. Ameri, P. Bäuerle, H. Ade, C. J. Brabec, *Adv. Energy Mater.* **2016**, 6, 1502579.

[56]    L. Ye, Y. Xiong, S. Li, M. Ghasemi, N. Balar, J. Turner, A. Gadisa, J. Hou, B. T. O'Connor, H. Ade, *Adv. Funct. Mater.* **2017**, 27, 1702016.

[57]    P. Müller-Buschbaum, *Adv. Mater.* **2014**, 26, 7692.

[58]   A. Hexemer, W. Bras, J. Glossinger, E. Schaible, E. Gann, R. Kirian, A. MacDowell, M. Church, B. Rude, H. Padmore, *Journal of Physics: Conference Series* **2010**, 247, 012007.

[59]   L. Yang, S. Zhang, C. He, J. Zhang, Y. Yang, J. Zhu, Y. Cui, W. Zhao, H. Zhang, Y. Zhang, Z. Wei, J. Hou, *Chem. Mater.* **2018**, 30, 2129.

[60]   K. Yamamoto, M. Shahiduzzaman, A. Yamada, T. Takaya, T. Chikamatsu, T. Koganezawa, M. Karakawa, T. Kuwabara, K. Takahashi, T. Taima, *Org. Electron.* **2018**, 63, 47.

[61]   D. M. DeLongchamp, R. J. Kline, A. Herzing, *Energy Environ. Sci.* **2012**, 5, 5980.

[62]   J. R. Tumbleston, B. A. Collins, L. Yang, A. C. Stuart, E. Gann, W. Ma, W. You, H. Ade, *Nat. Photonics* **2014**, 8, 385.

[63]   J. Min, Y. N. Luponosov, N. Gasparini, M. Richter, A. V. Bakirov, M. A. Shcherbina, S. N. Chvalun, L. Grodd, S. Grigorian, T. Ameri, S. A. Ponomarenko, C. J. Brabec, *Adv. Energy Mater.* **2015**, 5, 1500386.

[64]   S. Wood, D. O'Connor, C. W. Jones, J. D. Claverley, J. C. Blakesley, C. Giusca, F. A. Castro, *Sol. Energy Mater Sol. Cells* **2017**, 161, 89.

[65]   J. Wang, J. Zhang, Y. Xiao, T. Xiao, R. Zhu, C. Yan, Y. Fu, G. Lu, X. Lu, S. R. Marder, X. Zhan, *J. Am. Chem. Soc.* **2018**, 140, 9140.

[66]   B. Xie, R. Xie, K. Zhang, Q. Yin, Z. Hu, G. Yu, F. Huang, Y. Cao, *Nat. Commun.* **2020**, 11, 2871.

**For "Table of Content" use only**

**Baseplate Temperature-Dependent Vertical Composition Gradient in Pseudo-Bilayer Films for Printing Non-fullerene Organic Solar Cells**

Yina Zheng[1†], Rui Sun[1†], Meng Zhang[2], Zhihao Chen[3], Zhengxing Peng[4]*, Qiang Wu[1], Xinxin Yuan[1], Yue Yu[1], Tao Wang[1], Yao Wu[1], Xiaotao Hao[3], Guanghao Lu[2], Harald Ade[4]*, Jie Min[1,5,6]*

The baseplate temperature-dependent blend morphology of SD-processed organic solar cells at vertical and lateral scales was systematically studied, and the temperature-microstructure-performance relation was established.